On the study of keyhole-mode melting in selective laser melting process

K. Q. Le, C. Tang, C. H. Wong[1]

Singapore Centre for 3D Printing, School of Mechanical and Aerospace Engineering, Nanyang Technological University, 50 Nanyang Avenue, Singapore 639798, Singapore

[1]Corresponding author. Email address: chwong@ntu.edu.sg

ABSTRACT

A physics-based computational fluid dynamics (CFD) model was developed to simulate selective laser melting (SLM) process. The heat source model imitates the multiple reflections of the laser beam by using the Fresnel absorption function. The model is able to simulate the fluid flow and heat transfer of keyhole-mode laser melting process, which is validated by single track experiments. In addition, the simulation results show that the melt pool dynamics of the well-deep keyhole is unsteady as compared to the medium-deep keyhole. Different modes of fluid flow, such as downward flow, bottom backward flow, clockwise flow and top forward flow are noticed in the well deep keyhole melt pool. On the other hand, the melt pool dynamics of the medium-deep keyhole is more stable with two main flows of downward flow and backward flow. Furthermore, the model brings the benefit of predicting the keyhole-induced porosity within the solidified track.

Keywords: Additive manufacturing, selective laser melting, keyhole, Fresnel reflection, porosity.

1. INTRODUCTION

In recent years, selective laser melting (SLM) has become one of the most effective powder based additive manufacturing methods for metal parts. The technique allows three-dimensional (3D) objects with complex geometry to be generated, while achieving desirable quality under suitable printing process parameters [1]. Additionally, it was reported that the quality of the printed parts can be affected by 130 parameters, and among them, laser power, scanning speed, layer thickness, hatch spacing, and powder distribution are common parameters to be investigated [2]. Qiu *et al.* found that the area fraction of porosity of printed

samples is larger at high layer thickness and high scanning speed. For example, at 20 μm layer thickness, the area fraction of porosity is 0.09%. However, the area fraction of porosity can increase by 100-folds when the layer thickness is 100 μm [3]. Moreover, Yadroitsev *et al.* studied the influence of hatch spacing on the surface morphology [4]. The study found that the maximum distance of the hatch spacing should not exceed the average width of the continuous melt track to achieve smooth printed surface. Furthermore, the process parameters will directly affect the melt pool geometry. For instance at lower energy density such laser power of 100 W and laser scanning speed of 188 mm/s, the melt pool would be in conduction-mode in which the melt pool depth is shallow. However at high energy density – with the same laser power of 100 W but laser scanning speed of 100 mm/s, the melt pool is in keyhole-mode in which the melt pool depth is deeper [5].

Many experiments have validated the occurrence of keyhole-mode laser melting in the SLM process. Bertoli *et al.* carried out single melt track experiments of the stainless steel 316L powder (SS316L) with different laser powers and scanning speeds [6]. The study found that the melt pool can occur in the conduction- or keyhole-mode. In addition, King *et al.* performed experiments to determine the conditions under which keyhole-mode laser melting will occur for selectively laser melted SS316L [5]. However, it is difficult to investigate the dynamics of the keyhole-mode induced melt pool by employing experiments. Therefore, numerical simulations have been adopted to demonstrate the mechanisms and the defects in the keyhole-mode. For instance, Tang *et al.* explained the mechanisms of the molten flow during keyhole-mode laser melting [7]. The molten flow around the keyhole is intense and unsteady, and due to the vortex at the rear part of the melt pool, bubbles which can lead to pores are formed. Furthermore, Tan *et al.* also explained the formation of spherical and elliptical pore shapes [8]. As the gas near the bottom of the keyhole is likely to trap into the collapsing keyhole, and due to the effect of surface tension, it forms the spherical and elliptical pore shapes.

In fact, it is challenging to model the keyhole-mode laser melting that occurs during the SLM process. An adequate representation would require improvements on the model. Most simulation works assumed a constant absorption coefficient of the laser heat source [9-11]. However, as reported by Trapp *et al.*, the absorption coefficient is dependent on the laser power and scanning speed [12]. Therefore, the assumption

of constant absorption coefficient becomes inadequate at some regime, especially when the melt track is in the keyhole-mode. Furthermore in reality, multiple reflections of the laser in the keyhole determine how the energy is actually transferred. However, most simulation works assumed only the top surface of the powders covered by the laser beam spot is heated [10, 13]. Therefore, previous simulation studies of SLM are still incorrect in terms of the heat source.

While studies have been performed on the melting process of SLM, there is a lack of deep insight into the melt pool dynamics during keyhole-mode melting due to its high complexity. Therefore, this work aims to develop a ray-tracing model to simulate the multiple reflections of the laser rays in the keyhole-mode laser melting with high accuracy at different laser powers and scanning speeds. While the ray-tracing model has been widely employed in laser welding simulations [14, 15], only a handful of studies applied it in the simulation of SLM process [16]. Moreover, the mechanisms and dynamics of the keyhole-mode melting in the SLM process is also revealed in this work. Additionally, the model brings the possibility in predicting porosity formation observed in realistic experiments.

2. COMPUTATIONAL MODEL

In order to generate the powder bed, a discrete element method (DEM) model was used to simulate the free surface of the powder. The simulation was performed in LIGGGHTS® where the packing density of powder was achieved by calculating the motions of powder particles [17]. Firstly, the powder particles were dropped freely on the substrate due to the gravitational force. After the powders were deposited on the substrate, a blade was subsequently moved along the powder bed to form a uniform thickness of powder layer. Then, the powders' radii and coordinates were exported to OpenFOAM® [18] to generate powder particles on the substrate to perform computational fluid dynamics (CFD) simulation on laser interaction, phase change and melt pool dynamics.

2.1. Heat transfer and melt flow dynamics model

The CFD model was used to solve laser-powder bed interaction, phase change, heat and mass transfer, and fluid flow of the melt track. By employing volume of fluid (VOF) method, the model was able to capture the

interface between the metal and gas. The metallic phase and gaseous phase were determined by α_1 and $(1-\alpha_1)$ respectively. $\alpha_1 = 1$ indicates a cell completely occupied by the metallic phase and $\alpha_1 = 0$ represents a fully gaseous cell. A temperature dependent variable γ is employed to represent the solid or liquid state of the metal cells, and is described as [19]

$$\gamma = \begin{cases} 0, & T \le T_s \\ \dfrac{T - T_s}{T_l - T_s}, & T_s < T < T_l \\ 1, & T \ge T_l \end{cases}, \tag{1}$$

where T_s and T_l are solidus and liquidus temperature of the metal powder respectively and T is the temperature field of the computational domain. Hence, the volume fraction of solid metal f_s and liquid metal f_l are $\alpha_1(1-\gamma)$ and $\alpha_1\gamma$ respectively. Consequently, the material properties $\bar{\phi}$ of each cell is calculated as

$$\bar{\varphi} = \alpha_1(1-\gamma)\varphi_s + \alpha_1\gamma\varphi_l + (1-\alpha_1)\varphi_g, \tag{2}$$

where ϕ_s, ϕ_l, and ϕ_g are the material property in solid, liquid and gaseous phase respectively. The volume fraction of metallic phase satisfies the following conservation equation

$$\frac{\partial(\bar{\rho}\alpha_1)}{\partial t} + \nabla\cdot(\bar{\rho}\mathbf{u}\alpha_1) = 0, \tag{3}$$

where $\mathbf{u}$ is the flow velocity, t is time, and $\bar{\rho}$ is the volume average density.

The mass conservation is calculated as

$$\frac{\partial\bar{\rho}}{\partial t} + \nabla\cdot(\bar{\rho}\mathbf{u}) = 0, \tag{4}$$

while the momentum equation is considered as [3, 13]

$$\frac{\partial\bar{\rho}\mathbf{u}}{\partial t} + \nabla\cdot(\bar{\rho}\mathbf{u}\otimes\mathbf{u}) = -\nabla p + \nabla\cdot(\mu\nabla\mathbf{u}) - K_c\left[\frac{(1-f_l)^2}{f_l^3 + c_K}\right]\mathbf{u} + \bar{\rho}\mathbf{g} + \mathbf{F}_{st} + \mathbf{F}_M + \mathbf{P}_r, \tag{5}$$

where p is the pressure, μ is the dynamic viscosity, and $\mathbf{g}$ is gravitational acceleration. The Darcy's term, $-K_c\left[\frac{(1-f_l)^2}{f_l^3+c_K}\right]\mathbf{u}$, is the damping term in the mushy zone, where K_c and c_K are permeability coefficient and a small constant, respectively. The surface tension force $\mathbf{F}_{st}$ is written as

$$\mathbf{F}_{st} = \sigma\kappa\mathbf{n}\left|\nabla\alpha_1\right|\frac{2\overline{\rho}}{\rho_s(1-\gamma)+\rho_l\gamma+\rho_g}, \tag{6}$$

where σ, κ, and $\mathbf{n}$ are surface tension coefficient, surface curvature and unit normal respectively. $\left|\nabla\alpha_1\right|$ was adopted to transform an interfacial per unit into a volumetric surface force. The term $\frac{2\overline{\rho}}{\rho_s(1-\gamma)+\rho_l\gamma+\rho_g}$ is used to redistribute the interfacial force toward the heavier phase which is the metal phase. The surface tension σ of the metallic material is described as [20]

$$\sigma = \sigma_s^0 - A(T-T_s) - RT\Gamma_s \ln\left(1+k_1 a_i e^{-\Delta H^0/RT}\right), \tag{7}$$

where σ_s^0 is the surface tension of pure metal at the melting point (solidus temperature), A is the surface tension gradient for pure metal, R is gas constant, Γ_s is surface excess at saturation, k_1 is entropy factor, a_i is weight percent of sulfur, and ΔH^0 is the heat absorption. The unit normal vector and the curvature of metal/gas interface can be expressed as

$$\mathbf{n} = \frac{\nabla\alpha_1}{\left|\nabla\alpha_1\right|}, \text{ and} \tag{8}$$

$$\kappa = -\nabla\cdot\mathbf{n}. \tag{9}$$

The Marangoni force $\mathbf{F}_M$ is defined as

$$\mathbf{F}_M = \frac{d\sigma}{dT}\left(\nabla T - \mathbf{n}(\mathbf{n}\cdot\nabla T)\right)\left|\nabla\alpha_1\right|\frac{2\overline{\rho}}{\rho_s(1-\gamma)+\rho_l\gamma+\rho_g}, \tag{10}$$

where $\frac{d\sigma}{dT}$ describes the temperature coefficient of surface tension of SS316L. The recoil pressure $\mathbf{P}_r$ is described by

$$\mathbf{P}_r = 0.54P_0\exp\left[\frac{L_v M(T-T_v)}{RTT_v}\right]\mathbf{n}\left|\nabla\alpha_1\right|\frac{2\overline{\rho}}{\rho_s(1-\gamma)+\rho_l\gamma+\rho_g}, \tag{11}$$

where P_0 is ambient pressure, L_v is the latent of vaporization, T_v is the evaporation temperature, and M is the molar mass.

The energy conservation is expressed as [8, 21]

$$\frac{\partial \bar{\rho} h}{\partial t} + \nabla \cdot (\bar{\rho} \mathbf{u} h) = \nabla \cdot \left(D_f \nabla h \right) + q_{abs} - q_{loss} \left| \nabla \alpha_1 \right| \frac{2\bar{\rho}}{\rho_s (1-\gamma) + \rho_l \gamma + \rho_g}, \tag{12}$$

where h is the specific enthalpy, q_{abs} is the absorbed heat from the laser beam, and C_p is the heat capacity. The diffusion coefficient, D_f, is given as

$$D_f = (1-\alpha_1)\frac{k_g}{C_p} + \alpha_1 \frac{k_s \alpha_1 (1-\gamma_l) + k_l \alpha_1 \gamma}{C_p}, \tag{13}$$

where k and C_p are thermal conductivity and specific heat, respectively. The heat loss at the metal/gas interface is described by $q_{loss} = q_{conv} + q_{rad} + q_{evap}$ [7]. The convection heat loss is computed as $q_{conv} = h_c \left(T - T_\infty \right)$, where h_c is convection coefficient and T_∞ is ambient temperature. $q_{rad} = \varepsilon \sigma \left(T^4 - T_\infty{}^4 \right)$ is the radiation heat loss, where ε is emissivity and σ is the Stefan-Boltzmann constant. The evaporation heat loss is calculated as $q_{evap} = \frac{0.82 \Delta H_v^*}{\sqrt{2\pi MRT}} P_0 \exp\left[\frac{\Delta H_v^* \left(T - T_v \right)}{RTT_v} \right]$, where M is the molar mass [22].

In this model, the heat capacity C_p is described as [23]

$$C_p = \begin{cases} C_{ps0} + C_{psCoeff} T, & T \le T_s \\ \dfrac{h_s}{T_l - T_s}, & T_s < T < T_l \\ C_{pl}, & T \ge T_l \end{cases}, \tag{14}$$

where, $C_{ps} = C_{ps0} + C_{psCoeff} T$ is the temperature-dependent heat capacity of the solid phase, and h_s is the latent heat of fusion. Furthermore, the temperature T is calculated based on the enthalpy h. When the temperature is lower than the solidus temperature, the enthalpy h is calculated as

$$h(T) - h(T_{ref}) = \int_{T_{ref}}^{T} C_p dT, \tag{15}$$

where T_{ref} is the reference temperature which was set as 300 K. Thus, the relationship between the enthalpy h and the temperature T is described as [24]

$$T = \begin{cases} \dfrac{-C_{ps0} + \sqrt{{C_{ps0}}^2 + 2C_{psCoeff}(C_{ps0}T_{ref} + 0.5C_{psCoeff}T_{ref}^2 + h)}}{C_{psCoeff}} & , \quad h \le h(T_s) \\ T_s + \dfrac{h - h(T_s)}{h_s}(T_l - T_s) & , \quad h(T_s) < h \le h(T_s) + h_s \\ T_l + \dfrac{\left(h - h(T_s) - h_s\right)}{C_{pl}} & , \quad h > h(T_s) + h_s \end{cases} \tag{16}$$

where the $h(T_s) = C_{ps0}(T_s - T_{ref}) + 0.5C_{psCoeff}(T_s^2 - T_{ref}^2)$

The temperature field is calculated by solving Eqns. (14-15).

2.2. Laser heat source model

The laser heat source model plays a role in imitating the movement of a laser beam with the power of P_{laser} and the beam radius of r. The laser moves at a velocity of v_0, with the laser beam center at coordinates (x_0, z_0). The laser beam was assumed as a Gaussian heat source with the distribution factor f of two. The ray-tracing algorithm firstly identified all the metallic cells at the gas/metal interface cells. The initial laser rays were subsequently generated according to the laser beam profile. Finally, the ray-tracing procedure was performed to track the travel and reflection of laser rays. The details are described in the following sections.

a. Gas/metal interface cell identification

In the model, the gas/metal interface cells are identified by using the volume fraction of metallic phase α_1, and Fig. 1(a) illustrates the gas/metal interface cells of the powder bed. The cell is considered as a gas/metal interface cell when it satisfies the following conditions

$$\begin{cases} \alpha_1 \ge 0.5 \\ |\nabla \alpha_1| > \varepsilon / \Delta x = 0.05 / \Delta x \end{cases}, \tag{17}$$

where Δx is the cell width or so-called grid size, and ε is a small arbitrary number (0.05). Firstly, only those cells containing metal phases ($\alpha_1 \ge 0.5$) may absorb the power during laser scanning process. Secondly, as

for VOF method, the gradient of α_1 is inversely proportional to the grid size and is only non-zero at the interface. In this work, the gradient of α_1 can be evaluated by

$$\nabla \alpha_1 = \left(\frac{\partial \alpha_1}{\partial x}, \frac{\partial \alpha_1}{\partial y}, \frac{\partial \alpha_1}{\partial z} \right), \tag{18}$$

where

$$\left. \frac{\partial \alpha_1}{\partial x} \right|_{i,j,k} = \frac{\alpha_1|_{i+1,j,k} - \alpha_1|_{i-1,j,k}}{2\Delta x},$$

$$\left. \frac{\partial \alpha_1}{\partial y} \right|_{i,j,k} = \frac{\alpha_1|_{i,j+1,k} - \alpha_1|_{i,j-1,k}}{2\Delta x},$$

$$\left. \frac{\partial \alpha_1}{\partial z} \right|_{i,j,k} = \frac{\alpha_1|_{i,j,k+1} - \alpha_1|_{i,j,k-1}}{2\Delta x}.$$

Around the interface, α_1 typically changes from 0 to 1 within two or three cells. Therefore, the second condition can be used to find the interface.

b. Rays generation

The laser beam center was initially located at $c_{beam,0} = (x_0, z_0)$ and the laser beam plane was set parallel to the substrate plane. Starting from the center of the laser beam, the algorithm firstly searched for the cells within 1.6*r* of the beam as depicted in Fig. 2(a) in order to capture 99.44% of the total laser power. The rays from the laser were then generated for each cell. Each ray contains the information of ray center A_j^i, ray direction $\mathbf{u}_j^i$, times of reflection i^{th}, and laser ray power P_j^i, where j indicates ordinal ray number, and i represents the number of times the laser ray is reflected, where $i = 0$ represents an incident laser ray without reflection. For stainless steel 316L (SS316L) with the reflective index of $n = 3.24 + 4.28i$, the absorption coefficient is around 0.3 [23]. After a laser ray undergoes 13 times of reflection, the remaining power becomes negligible (around 1%) as compared to the initial ray power. Therefore in this work, the ray tracing procedure for a laser ray terminates when the times of reflection reaches 13. Initially, all rays have an initial direction of $\mathbf{u}_j^0 = (0,-1,0)$. Moreover, the initial power P_j^0 of each ray is given by

$$P_j^0 = \frac{fP_{laser}}{\pi r^2}\exp\left[-f\frac{\left(x_{cj}-v_0t-x_0\right)^2+\left(z_{cj}-z_0\right)^2}{r^2}\right]\Delta x^2 . \tag{19}$$

c. The interaction between the ray and the cells

A single laser ray is employed to explain the absorption and reflection of the laser ray as shown in Fig. 1. The laser ray has the starting point of $A_j^i=\left(x_j^i,y_j^i,z_j^i\right)$ with the unit vector of the laser ray direction of $\mathbf{u}_j^i=\left(ux_j^i,uy_j^i,uz_j^i\right)$ as shown in Fig. 1(a). The vector from the center of the gas/metal interface cell *k*, which is denoted by $B_k=\left(x_{B,k},y_{B,k},z_{B,k}\right)$, to the starting of ray *j* is therefore calculated as

$$\mathbf{d}_{2k,j}=\left(x_{B,k}-x_j^i,y_{B,k}-y_j^i,z_{B,k}-z_j^i\right). \tag{20}$$

The unit vector from A_j^i to B_k is defined as

$$\mathbf{u}_{k,j}^i=\frac{\mathbf{d}_{2k,j}}{\left|\mathbf{d}_{2k,j}\right|} . \tag{21}$$

The angle θ_j^i between the vector $\mathbf{u}_j^i$ and $\mathbf{u}_{k,j}^i$ is expressed as

$$\theta_j^i=\arccos\left(\frac{\mathbf{u}_j^i\mathbf{u}_{k,j}^i}{\left|\mathbf{u}_j^i\right|\left|\mathbf{u}_{k,j}^i\right|}\right). \tag{22}$$

Therefore, the perpendicular distance from B_k to ray *j* is given as

$$d_{1k,j}^i=\left|\mathbf{d}_{2k,j}^i\right|\sin\left(\theta_j^i\right). \tag{23}$$

Then, the program searches for the gas/metal interface cells along the ray path. Cell *k* is considered as gas/metal interface cell along the ray path when the distance $d_{1k,j}^i\le\sqrt{3}/2\,\Delta x$ as depicted in Fig. 1(b). Among the gas/metal interface cells along the ray path, the cell with the shortest $\left|\mathbf{d}_{2k,j}^i\right|$ is chosen as corresponding interface cell where the laser heat source is mainly absorbed as illustrated in Fig. 1(c). Subsequently, the program calculates the Fresnel absorption coefficient which is computed as [25]

$$\eta=1-\frac{1}{2}\left[\frac{(\mathrm{Re}_{ref}\cos\psi_j^i-1)^2+(\mathrm{Im}_{ref}\cos\psi_j^i)^2}{(\mathrm{Re}_{ref}\cos\psi_j^i+1)^2+(\mathrm{Im}_{ref}\cos\psi_j^i)^2}+\frac{(\mathrm{Re}_{ref}-\cos\psi_j^i)^2+\mathrm{Im}_{ref}\,\mathrm{Im}_{ref}}{(\mathrm{Re}_{ref}+\cos\psi_j^i)^2+\mathrm{Im}_{ref}\,\mathrm{Im}_{ref}}\right], \tag{24}$$

where Re_{ref} and Im_{ref} are the reflective index *n* of the material. The symbol ψ_j^i is the angle between the incident laser ray and the surface normal vector $\mathbf{n}_k$ of cell *k*, and it is described as [15]

$$\psi_j^i = \arccos(-\mathbf{u}_j^i \mathbf{n}_k). \tag{25}$$

As a result, the corresponding interface cell at which the laser ray directly irradiates and its neighbouring cells will absorb the laser power of $P_{j,k,abs}^i = \eta P_j^i$ (see Fig. 1(c)) based on the distribution index given as [15]

$$w_k = \begin{cases} 1, & k \equiv (m,n,p) \\ 0.3, & k \equiv (m\pm1,n,p),(m,n\pm1,p),(m,n,p\pm1) \end{cases} \tag{26}$$

where (m,n,p) denotes the corresponding interface cell, and the neighboring cells are $(m\pm1,n,p)$, $(m,n\pm1,p)$ and $(m,n,p\pm1)$ as depicted in Fig. 3. The heat source from ray *j* is applied to each cell and is calculated as

$$q_{j,k,abs} = \frac{\eta P_j^i \alpha_{1,k}}{\alpha_1(m,n,p) + 0.3\alpha_1(m\pm1,n,p) + 0.3\alpha_1(m,n\pm1,p) + 0.3\alpha_1(m,n,p\pm1)}, \tag{27}$$

if the cell is the corresponding interface cell. However, if the cell is a neighboring cell, the heat source is then computed as

$$q_{j,k,abs} = \frac{0.3\eta P_j^i \alpha_{1,k}}{\alpha_1(m,n,p) + 0.3\alpha_1(m\pm1,n,p) + 0.3\alpha_1(m,n\pm1,p) + 0.3\alpha_1(m,n,p\pm1)}. \tag{28}$$

Hence, the total heat absorbed into cell *k* is $q_{k,abs} = \sum_{j=1}^{\max j} q_{j,k,abs}$. This value is then used in Eqn. (12) to calculate the temperature field.

Furthermore, the information of the laser ray *j* at the reflected time $(i+1)^{th}$ is updated, with the laser power of $P_j^{i+1} = (1-\eta)P_j^i$, the starting point $A_j^{i+1} \equiv B_k$ (see Fig. 1(d)). Moreover, the direction of the laser ray *j* at the reflection $(i+1)^{th}$ is calculated as [14]

$$\mathbf{u}_j^{i+1} = \mathbf{u}_j^i - 2(\mathbf{u}_j^i \mathbf{n}_k)\mathbf{n}_k, \text{ and } \mathbf{u}_j^{i+1} = \frac{\mathbf{u}_j^{i+1}}{\left|\mathbf{u}_j^{i+1}\right|} \tag{29}$$

The reflection process will continue until the laser ray power is close to zero or the number of reflection is greater than 13.

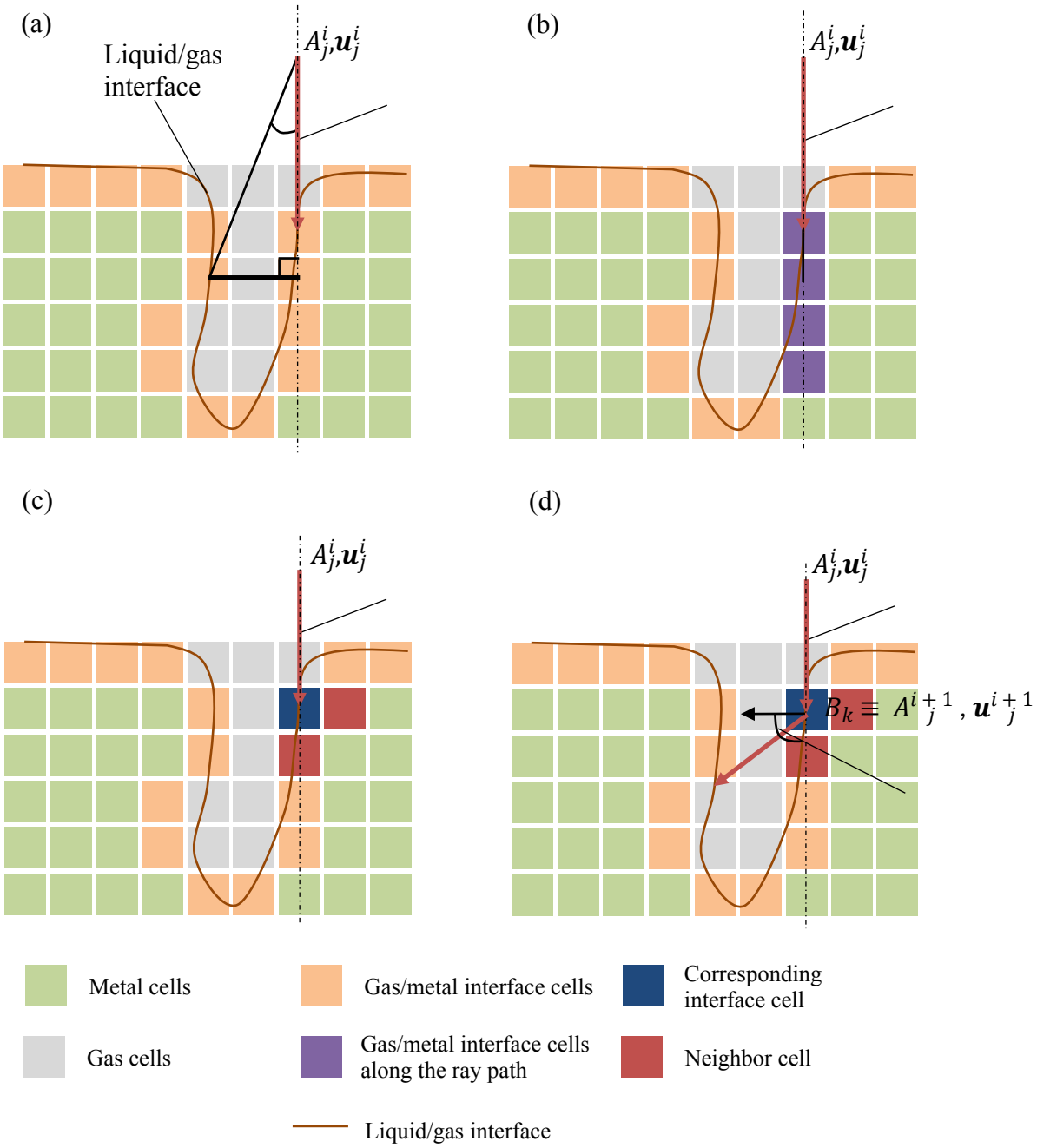

Fig. 1: Schematic of (a) gas/metal interface cells, (b) gas/metal interface cells along the laser beam, (c) incident cell and the neighbor cells and (d) reflected laser beam.

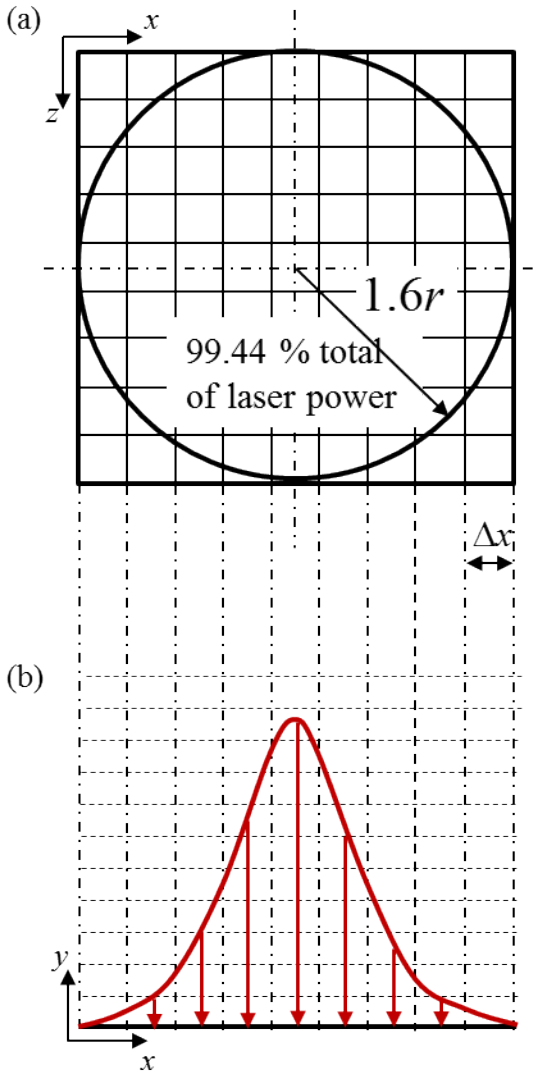

Fig. 2: Schematic diagram of (a) the beam calculating area and (b) sub-rays at the center of the laser beam.

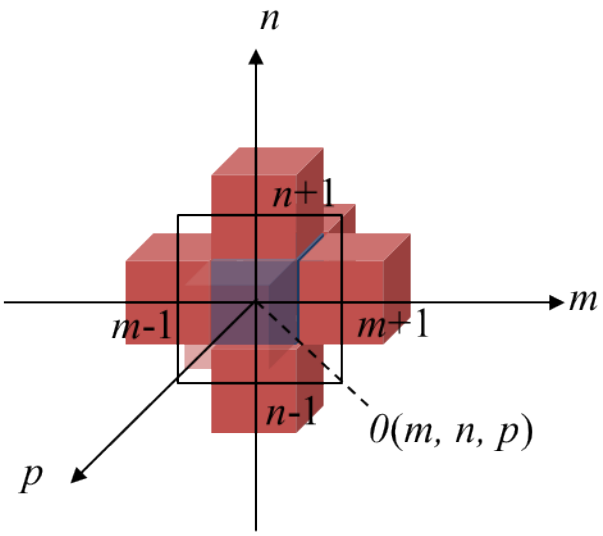

Fig. 3: Schematic of corresponding interface cell and neighbor cells

2.3. Simulation setup and material properties

The main objective of this study is to examine the consistency between simulations and experiments in the keyhole-mode melting in SLM process. The experimental work by Bertoli *et al.* was chosen for comparison [6]. The experiment used gas-atomized Micro-Melt® SS316L powder ranging from 16 to 45 μm in diameter. A near-Gaussian laser beam with diameter of 55 μm was employed and the layer thickness of the powder bed was kept consistent at 75 μm.

Simulations of single-track melting were performed to model the experiment accordingly. The simulations were carried out with different laser powers and laser scanning speeds as listed in Table 1. The three-dimensional (3D) simulation domain had a dimension of $x \times y \times z = 1920 \times 600 \times 400$ μm^3, with the direction of the gravity along y-axis. The simulation domain comprised a 400 μm tall substrate, 75 μm thick layer of powder bed, and a 125 μm tall layer of air above the powder bed. The powder was assumed to be spherical in shape and follows the Gaussian distribution with the powder diameter ranging from 16 to 45 μm. The cell size of $4 \times 4 \times 4$ μm^3 was used in the model. The initial temperature of the domain was set at 300 K. In addition, the laser beam radius was set as 27.5 μm, which follows a Gaussian distribution with the distribution factor of two.

Table 1: Laser powers and scanning speeds used in the simulation of single-track melting

Sample	Laser power (W)	Scanning speed (mm/s)	Energy density (J/mm^3)
A	300	1500	48
B	400	2000	48
C	300	900	81
D	500	1500	81
E	300	750	97
F	300	600	121
G	400	800	121
H	200	300	162
K	300	450	162

In the simulation, the material properties of SS316L were modelled as temperature-dependent and can be determined by $\Phi = a + bT + cT^2$ [23, 27], where Φ is the material property, and *a*, *b*, and *c* are the constant coefficients listed in Table 2.

Table 2: Material properties of SS316L and coefficients applied in the simulation

Material property	Symbol	Value	Ref
Density of solid metal (kg/m^3)	ρ_s	7900	[28]
Density of liquid metal (kg/m^3)	ρ_l	$7433 + 0.0393T - 1.8\times10^{-4}T^2$	[23]
Specific heat of solid metal ($Jkg^{-1}K^{-1}$)	C_{ps}	$462 + 0.134T$	[23]
Specific heat of liquid metal ($Jkg^{-1}K^{-1}$)	C_{pl}	775	[23]
Thermal conductivity of solid metal ($Wm^{-1}K^{-1}$)	k_s	$9.248 + 0.01571T$	[23]

Thermal conductivity of liquid metal ($Wm^{-1}K^{-1}$)	k_l	$12.41+0.003279T$	[23]
Thermal conductivity of air ($Wm^{-1}K^{-1}$)	k_g	0.03	[29]
Boiling temperature (K)	T_v	3090	[7]
Solidus temperature (K)	T_s	1658	[7]
Liquidus temperature (K)	T_l	1723	[7]
Molar mass ($kgmol^{-1}$)	M	0.05593	[7]
Viscosity of liquid metal ($kgm^{-1}s^{-1}$)	μ	6×10^{-3}	[28]
Permeability coefficient ($kgm^{-3}s^{-1}$)	K_C^0	1×10^{12}	
Surface tension of pure metal at melting point (Nm^{-1})	σ_s^0	1.943	[20]
Temperature coefficient of surface tension ($Nm^{-1}K^{-1}$)	A	4.3×10^{-4}	[20]
Surface excess at saturation	Γ_s	1.3×10^{-8}	[20]
Entropy factor	k_1	0.00318	[20]
Weight percent of sulfur (%)	a_i	0.00	-
Heat of fusion (m^2s^{-2})	h_s	2.7×10^5	[30]
Latent heat of vaporization (m^2s^{-2})	L_v	7.45×10^6	[7]
Atmosphere pressure (Nm^{-2})	P_0	101,000	[7]
Universal gas constant ($kgm^2s^{-2}K^{-1}mol^{-1}$)	R	8.314	[7]
Stefan-Boltzmann's constant ($Wm^{-2}K^{-4}$)	σ_s	5.67×10^{-8}	[7]
Emissivity	ε	0.4	[9]
Convection coefficient ($kgs^{-3}K^{-1}$)	h_c	80	[7]
Power distribution factor	f	2	[6]
Beam radius (μm)	r	27.5	[6]
Reflective index of SS316L at wavelength of 1 μm	n	3.27+*i*4.48	[31]

3. RESULTS AND DISCUSSION

3.1. Validation of the model

In this work, the melt pool depths and widths were used to determine the accuracy of the model. The melt pool depths and widths were measured at different cross-sections at x = 1100, 1200, and 1300 μm. The melt pool depths were measured from the top surface of the substrate, and the melt pool widths were taken where its width is largest at the top surface of the substrate. The average values of the melt pool depths and widths were extracted and compared with the experimental values from the work by Bertoli *et al.* [6] as listed in Table 3.

Table 3: The comparison of the melt pool depth and width in the simulation and the experiment [6]

Sample	Depth			Width		
	Simulation (μm)	Experiment [6] (μm)	Deviation, □ (%)	Simulation (μm)	Experiment [6] (μm)	Deviation, □ (%)
A	60 ± 0	50	20.00	86 ± 2	85 ± 11	1.18
B	57.3 ± 2.7	64	10.47	92 ± 4	105 ± 18	12.38
C	120 ± 0	128	6.25	100 ± 8	109 ± 21	8.26
D	112 ± 0	123	8.94	100 ± 4	99 ± 33	1.01
E	152 ± 0	146	4.12	112 ± 4	115 ± 25	2.61
F	198 ± 0	198	0.00	114 ± 2	130 ± 29	12.31
G	194 ± 2	220	11.82	108 ± 4	120 ± 22	10.00
H	276 ± 4	266	3.76	110 ± 2	130 ± 10	15.38
K	278 ± 6	302	7.95	110 ± 2	140 ± 25	21.43

From the data shown in Table 3, the deviations between the simulated melt pool depths and widths and the experiments are in most cases smaller than 15%. Two cases, however, exhibit deviations larger than 15% such as the depth of sample A and width of the sample K. One possible reason could be due to the constant reflective index used in the model, while in reality this reflective index is dependent on the temperature of

the material [32]. As a result, the model is unable to produce the melt pool width as closely to the experiment when the laser penetrates intensively into the substrate.

Furthermore, the effect of energy density on melt pool depth was also simulated as shown in Fig. 4 which depicts the melt pool geometry of the samples with the same laser power of 300 W at different energy densities of 48, 81, 97, 121, and 162 J/mm^3, respectively. At low energy density of 48 J/mm^3 (see sample A of Fig. 4(a)), the melt pool is shallow with a depth of 60 µm. The melt pool depth, however, increases with higher energy density. For example, when the energy density increases from 81 J/mm^3 (see Fig. 4(b)) to 162 J/mm^3 (see Fig. 4(e)), the melt pool depth also increases from 128 µm to 278 µm.

Separately, a similar trend is observed when the laser power is increased to 400 W which produces deeper melt pool when higher energy density is applied (see Table 1). The melt pool depth of sample B with energy density of 48 J/mm^3 is 57.3 µm, while the melt pool depth of the sample G with the energy density of 121 J/mm^3 is 192 µm. Therefore, the energy density greatly affects the depth of the melt pool, which is consistent with the experiment [6].

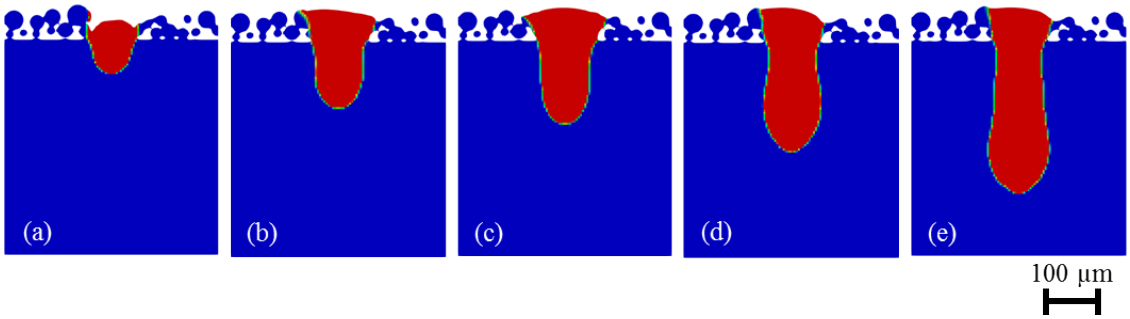

Fig. 4: Melt pool geometry of the sample (a) A, (b) C, (c) E, (d) F, and (e) K at the cross-section of x = 1000 µm.

3.2. Melt pool dynamics in the keyhole mode

The dynamics of the keyhole-mode melting is demonstrated in this section. Two types of keyhole-mode melting are investigated, namely the medium-deep keyhole and well-deep keyhole. In this study, a melt pool depth that is three times greater than the focused laser beam diameter is considered as the deep keyhole. Two samples C and K at different energy densities of 81 and 162 J/mm^3 were investigated in this study. Sample C, whose melt pool depth is 120 μm, is represented as a medium-deep keyhole. Sample K, whose melt pool depth is 278 μm, is considered as a well-deep keyhole.

Fig. 5 depicts the melt pool dynamics of the medium-deep keyhole (sample C). There exists two main dominant flow directions in the melt pool: (1) the downward flow from the top surface to the bottom of the front wall of the keyhole (see arrow *1* in Fig. 5) due to the recoil pressure penetrating strongly into the substrate and (2) the backward flow moving from the bottom of the keyhole opposite to the scanning direction (see arrow *2* in Fig. 5). As the recoil pressure penetrates into the substrate, the molten liquid is pushed to the tail of the melt track maintaining an opened large keyhole and keeping the distance between the front and rear wall of the keyhole at about 200 μm. This large distance prevents the molten metal from the rear wall to flow back to the front to merge with the front keyhole wall. Therefore, this inhibits the formation of bubbles, which in turn reduces the formation of pores.

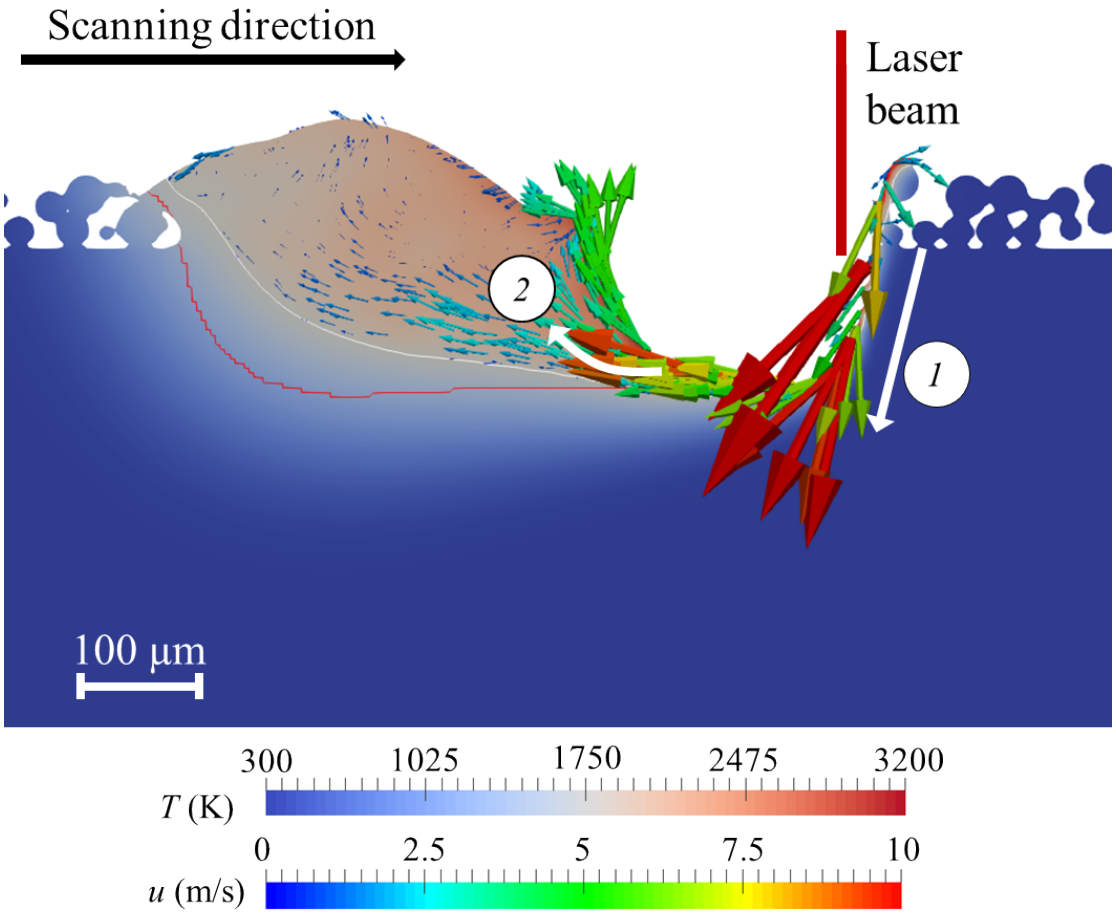

Fig. 5: The temperature and velocity distribution of the medium-deep keyhole mode at the cross-section of z = 200 µm at t = 600 µs of sample C. The red contour represents the area have been melted, while the white contour depicts the area which has the temperature larger than the liquidus temperature. The white arrows represent main stream flows in the melt pool.

On the other hand, the melt pool dynamics in the case of well-deep keyhole is more turbulent as depicted in Fig. 6. Different molten directions including the downward flow, bottom backward flow, clockwise flow, and top forward flow can be observed. Such molten flows were also observed in the laser welding simulation carried out by Lin *et al.* [14]. Similar to the medium-deep keyhole, the downward flow in the front keyhole wall (see arrow *1* of Fig. 6(c)) is attributed to the recoil pressure. In addition, this recoil pressure also plays a role in pushing the molten metal from the keyhole moving in the opposite direction of the scanning direction, forming the bottom backward flow as depicted in Fig. 6(a) and Fig. 6(c) (arrow *2*). Nevertheless,

as the keyhole is very deep, the molten metal can only accumulate at the top of the keyhole and flows downward back to the keyhole as observed in the Fig. 6(b). At the same time, the molten metal at the bottom of the keyhole continues to flow upward along the melt pool boundary under the effect of the recoil pressure. These two different metal flows enhance the generation of a clockwise flow [24]. As the clockwise flow (arrow *3*) becomes prevalent as shown in Fig. 6(c), it leads to a larger bulge forming at the top of the keyhole. This cycle of clockwise flow continues and as a result, the molten metal from the rear wall will eventually flow to the front and merge with the front keyhole.

Furthermore, the laser rays are entrapped at the bottom of the well deep keyhole [33] due to its deep and narrow geometry. As such, the reflections of the laser rays occur mostly at the bottom of the keyhole resulting in a larger bottom and a narrower top as depicted in Fig. 6(c). At the same time, as the laser continues to scan, a top forward flow is formed as shown by arrow *4* of Fig. 6(c). As the surface tension force plays a role of preventing the formation of keyhole, therefore, the surface tension force causes the molten metal to move forward to fill up the keyhole forming a top forward flow. Additionally, the clockwise flow induces the formation of bubbles. In many cases, bubbles that are caught in the liquid/gas interface can escape from the melt pool. However, some bubbles are unable to escape from the melt pool and they become pores when the melt pool solidifies.

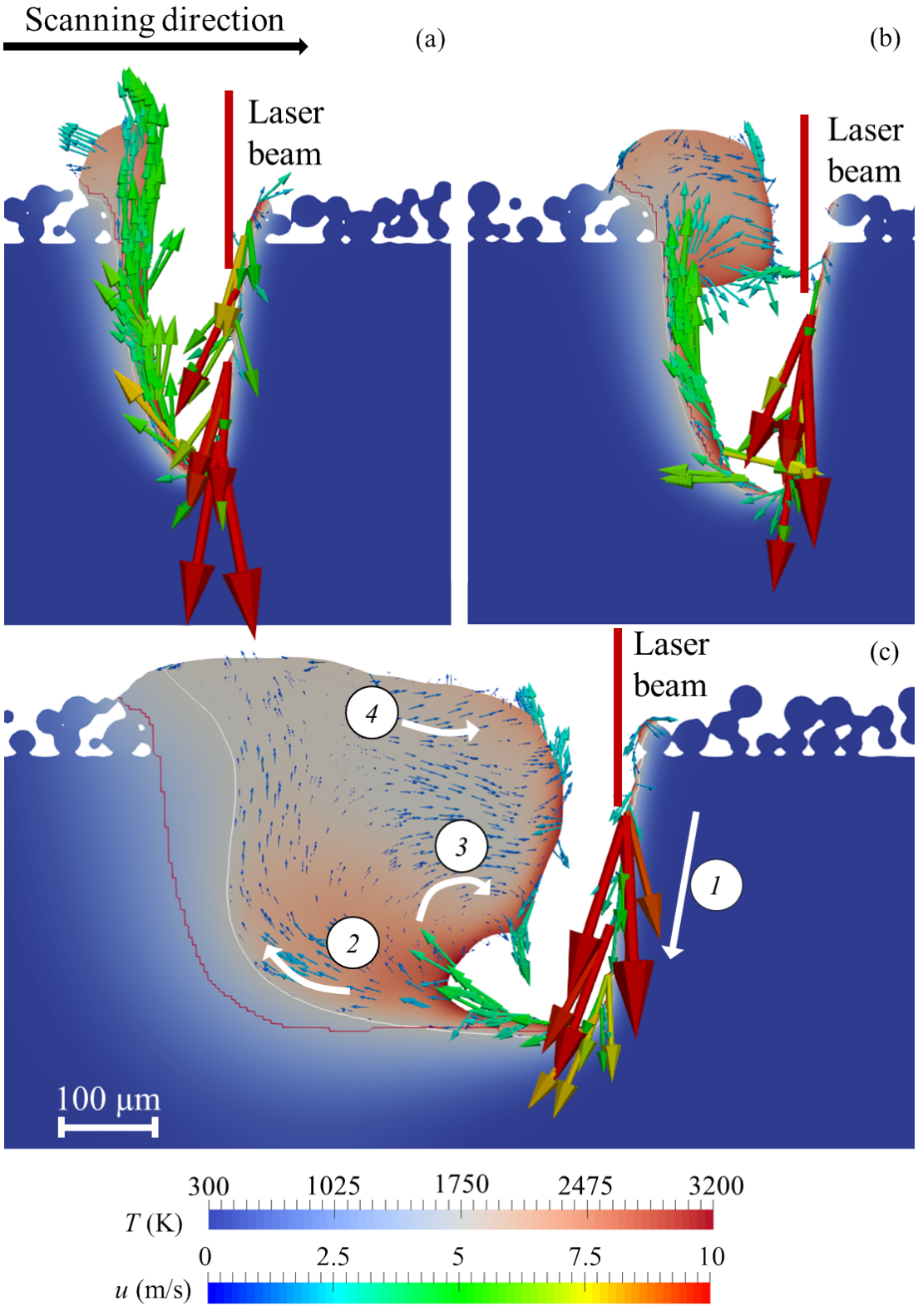
Scanning direction
(a)
(b)
Laser beam
Laser beam
Laser beam
(c)
4
3
2
1
100 µm
300
1025
1750
2475
3200
T (K)
0
2.5
5
7.5
10
u (m/s)

Fig. 6: The temperature and velocity distribution of the well-deep keyhole mode at the cross-section of z = 200 μm, at (a) t = 190 μs, (b) t = 270 μs, and (c) t = 980 μs of the sample K. The red contour represents the area have been melted, while the white contour depicts the area which has the temperature larger than the liquidus temperature. The white arrows represent main stream flows in the melt pool.

3.3. Keyhole-induced pores in well-deep keyholes

Experiments were carried out to observe the formation of the keyhole-induced pores in well deep keyholes. Laser power of 300 W and scanning speed of 300 mm/s were employed to print a single melt track of SS316L powder (size ranging from 20 to 53 μm) in SLM® 280 HL. The printed track was then cut at different cross-sections and observed under the optical microscope. Simulations were carried out to observe the pores in the melt track too. The same experimental process parameters were applied to the simulation and laser beam spot size of 80 μm was adopted. It was found that similar pore can be observed in the simulation as depicted in Fig. 7. The pore is in spherical shape and is consistent with the observations in ref. [7]. The dynamics of the pore observed in the simulation in Fig. 7 is illustrated in Fig. 8. A bubble is first formed in the keyhole and is attempting to move out of the keyhole at t = 1770 μs as depicted in Fig. 8(a). The bubble then exists in the melt pool (Fig. 8(b)) before it reaches the melt pool boundary at t = 1950 μs (see Fig. 8(c)). When the bubble reaches the melt pool boundary, it starts to solidify and becomes a pore as observed in Fig. 8(d).

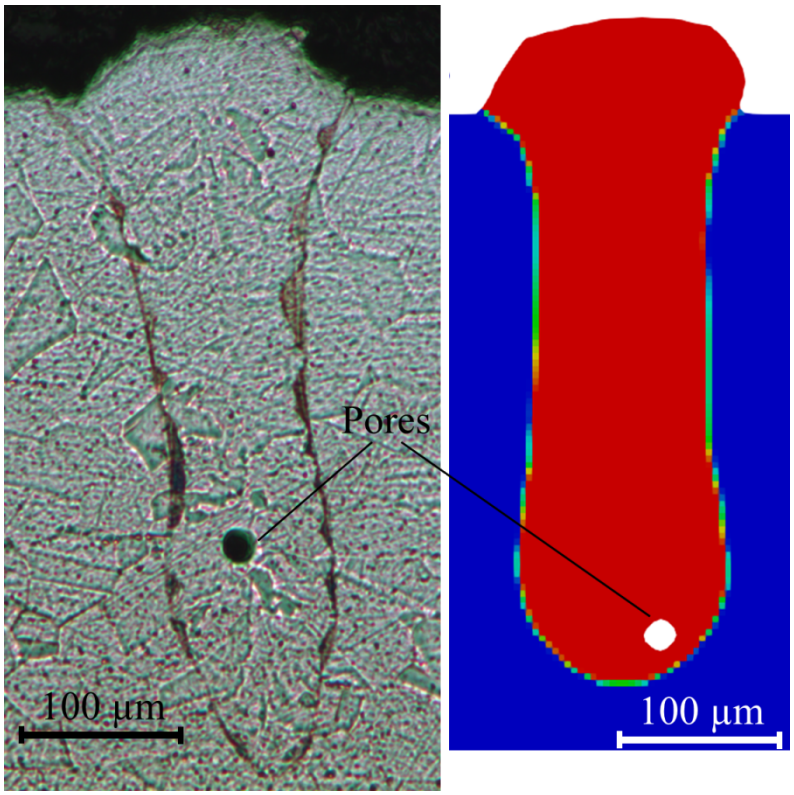

Fig. 7: The observation of pore in the (a) experiment and (b) simulation with laser power of 300 W, scanning speed of 300 mm/s, and beam diameter of 80 µm.

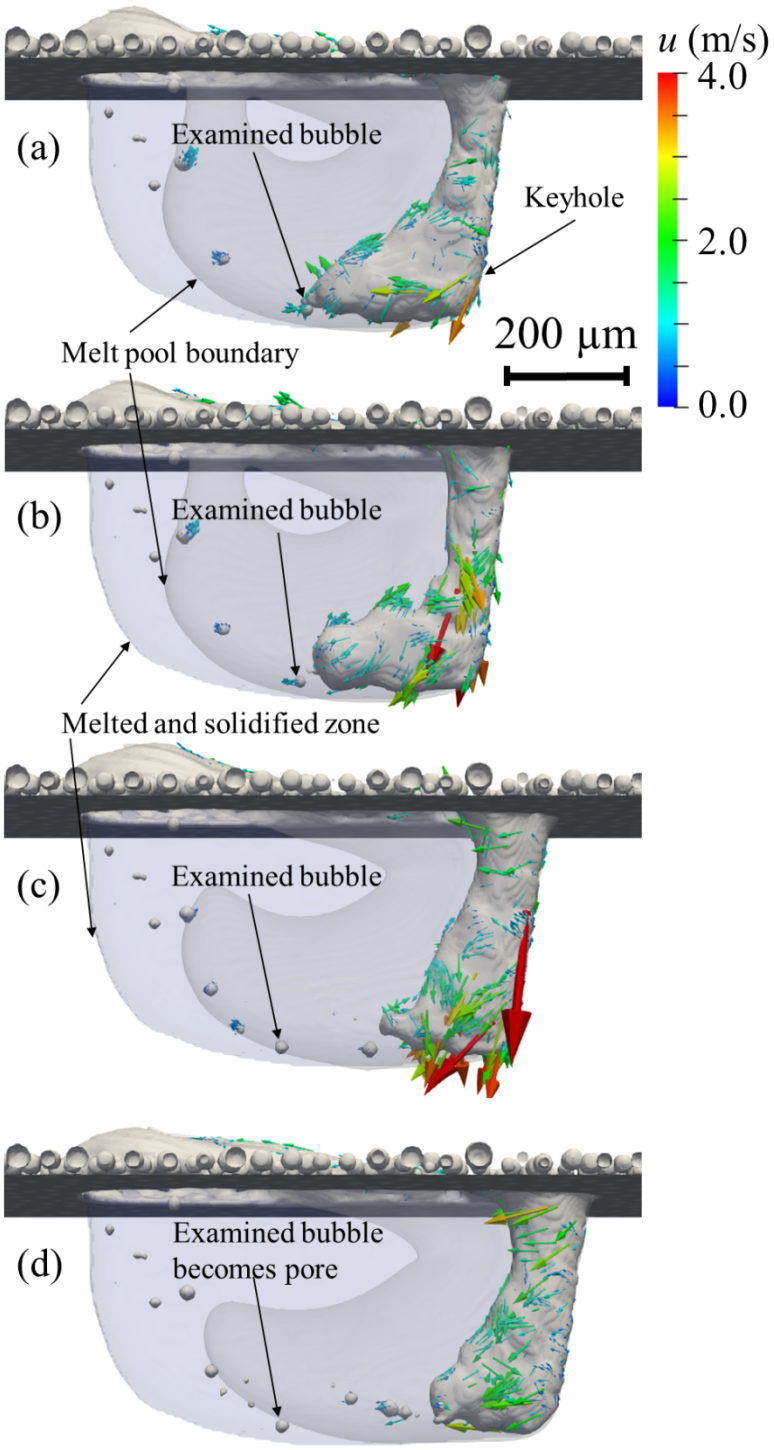

Fig. 8: Dynamics of examined bubble (a) at t = 1770 µs, (b) at t = 1780 µs, (c) at t = 1950 µs, and (d) at t = 2150 µs.

4. CONCLUSIONS

This work shares the computational model to simulate keyhole-mode melting in SLM process. The simulation results elucidated the melt pool dynamics of the medium-deep keyhole and well-deep keyhole. It shows that the well-deep keyhole exhibits unstable melt pool dynamics, causing the collapse of the keyhole and the formation of the bubble, which leads to pores. On the other hand, the molten flow is more stable in the case of medium-deep keyhole. Two main flows, downward flow at the front wall and backward flow at the rear keyhole, exist in the medium-deep keyhole, maintaining the stability of the melt pool. Hence, it prevents the formation of entrapped bubbles and reduce the appearance of pores. Furthermore, the model also brings the benefit in predicting the keyhole-induced porosity found in the solidified melt track.

ACKNOWLEDGEMENT

The authors acknowledged the support by the National Research Foundation, Prime Minister's Office, Singapore under its Medium-Sized Centre funding scheme. The authors thank Dr. Mingxuan Gan for helping in printing the samples.

REFERENCES

[1] C. W. J. Lim, K. Q. Le, Q. Lu, C. H. Wong, "An Overview of 3-D Printing in Manufacturing, Aerospace, and Automotive Industries," *IEEE Potentials*, vol. 35, p. 18-22, 2016.

[2] I. Yadroitsau, "Selective Laser Melting: Direct Manufacturing of 3D-Objects by Selective Laser Melting of Metal Powders," *Lambert Academic Publishing*, 2009.

[3] C. Qiu, C. Panwisawas, M. Ward et al., "On the Role of Melt Flow into the Surface Structure and Porosity Development during Selective Laser Melting," *Acta Materialia*, vol. 96, p. 72-79, 2015.

[4] I. Yadroitsev, and I. Smurov, "Surface Morphology in Selective Laser Melting of Metal Powders," *Physics Procedia*, vol. 12, p. 264-270, 2011.

[5] W. E. King, H. D. Barth, V. M. Castillo et al., "Observation of Keyhole-mode Laser Melting in Laser Powder-bed Fusion Additive Manufacturing," *Journal of Materials Processing Technology*, vol. 214, p. 2915-2925, 2014.

[6] U. Scipioni Bertoli, A. J. Wolfer, M. J. Matthews et al., "On the Limitations of Volumetric Energy Density as a Design Parameter for Selective Laser Melting," *Materials & Design*, vol. 113, p. 331-340, 2017.

[7] C. Tang, J. L. Tan, and C. H. Wong, "A Numerical Investigation on the Physical Mechanisms of Single Track Defects in Selective Laser Melting," *International Journal of Heat and Mass Transfer*, vol. 126, p. 957-968, 2018.

[8] J. Tan, C. Tang, and C. Wong, "A Computational Study on Porosity Evolution in Parts Produced by Selective Laser Melting," *Metallurgical and Materials Transactions A*, vol. 49, p. 3663-3673, 2018.

[9] S. A. Khairallah, A. T. Anderson, A. Rubenchik et al., "Laser Powder-bed Fusion Additive Manufacturing: Physics of Complex Melt Flow and Formation Mechanisms of Pores, Spatter, and Denudation Zones," *Acta Materialia*, vol. 108, p. 36-45, 2016.

[10] Y. S. Lee, and W. Zhang, "Modeling of Heat Transfer, Fluid Flow and Solidification Microstructure of Nickel-base Superalloy Fabricated by Laser Powder Bed Fusion," *Additive Manufacturing*, vol. 12, p. 178-188, 2016.

[11] C. Panwisawas, C. Qiu, M. J. Anderson et al., "Mesoscale Modelling of Selective Laser Melting: Thermal Fluid Dynamics and Microstructural Evolution," *Computational Materials Science*, vol. 126, p. 479-490, 2017.

[12] J. Trapp, A. M. Rubenchik, G. Guss et al., "In Situ Absorptivity Measurements of Metallic Powders during Laser Powder-bed Fusion Additive Manufacturing," *Applied Materials Today*, vol. 9, p. 341-349, 2017.

[13] K. Q. Le, C. Tang, and C. H. Wong, "A Study on the Influence of Scanning Strategies on the Levelness of the Melt Track in Selective Laser Melting Process of Stainless Steel Powder," *JOM*, vol. 70, p. 2082-2087, 2018.

[14] R. Lin, H.-p. Wang, F. Lu et al., "Numerical Study of Keyhole Dynamics and Keyhole-Induced Porosity Formation in Remote Laser Welding of Al Alloys," *International Journal of Heat and Mass Transfer*, vol. 108, pp. 244-256, 2017.

[15] W.-I. Cho, S.-J. Na, M.-H. Cho et al., "Numerical Study of Alloying Element Distribution in CO2 Laser–GMA Hybrid Welding," *Computational Materials Science*, vol. 49, p. 792-800, 2010.

[16] Y. Yang, D. Gu, D. Dai et al., "Laser Energy Absorption Behavior of Powder Particles using Ray Tracing Method during Selective Laser Melting Additive Manufacturing of Aluminum Alloy," *Materials & Design*, vol. 143, p. 12-19, 2018.

[17] C. Kloss, C. Goniva, A. Hager et al., "Models, Algorithms and Validation for Opensource DEM and CFD–DEM," *Progress in Computational Fluid Dynamics*, vol. 12, p. 140-152, 2012.

[18] H. G. Weller, G. Tabor, H. Jasak et al., "A Tensorial Approach to Computational Continuum Mechanics using Object-Oriented Techniques," *Computers in Physics*, vol. 12, p. 620-631, 1998.

[19] F. Rösler, and D. Brüggemann, "Shell-and-Tube Type Latent Heat Thermal Energy Storage: Numerical Analysis and Comparison with Experiments," *Heat and Mass Transfer*, vol. 47, p. 1027, 2011.

[20] M. H. Cho, and D. F. Farson, "Understanding Bead Hump Formation in Gas Metal Arc Welding using a Numerical Simulation," *Metallurgical and materials transactions B*, vol. 38, p. 305-319, 2007.

[21] W. Yan, W. Ge, Y. Qian et al., "Multi-Physics Modeling of Single/Multiple-Track Defect Mechanisms in Electron Beam Selective Melting," *Acta Materialia*, vol. 134, p. 324-333, 2017.

[22] J. Y. Lee, S. H. Ko, D. F. Farson et al., "Mechanism of Keyhole Formation and Stability in Stationary Laser Welding," *Journal of Physics D: Applied Physics*, vol. 35, p. 1570, 2002.

[23] L. Huang, X. Hua, D. Wu et al., "Numerical Study of Keyhole Instability and Porosity Formation Mechanism in Laser Welding of Aluminum Alloy and Steel," *Journal of Materials Processing Technology*, vol. 252, p. 421-431, 2018.

[24] X. Li, and W. Tan, "Numerical Investigation of Laser Absorption by Metal Powder Bed in Selective Laser Sintering Processes," *Proceedings of the 27th Annual International Solid Freeform Fabrication Symposium – An Additive Manufacturing Conference*, p. 219-235, 2016.

[25] C. D. Boley, S. A. Khairallah, and A. M. Rubenchik, "Calculation of Laser Absorption by Metal Powders in Additive Manufacturing," *Applied Optics*, vol. 54, p. 2477-2482, 2015.

[26] M. X. Gan, and C. H. Wong, "Practical Support Structures for Selective Laser Melting," *Journal of Materials Processing Technology*, vol. 238, p. 474-484, 2016.

[27] V. Bobkov, L. Fokin, E. Petrov et al., "Thermophysical Properties of Materials for Nuclear Engineering: a Tutorial and Collection of Data," International Atomic Energy Agency, Vienna, Austria, 2008.

[28] L. Han, F. W. Liou, and S. Musti, "Thermal Behavior and Geometry Model of Melt Pool in Laser Material Process," *Journal of Heat Transfer*, vol. 127, p. 1005-1014, 2005.

[29] Y. S. Touloukian, P. Liley, and S. Saxena, “Thermophysical Properties of Matter-the TPRC Data Series, Volume 3, Thermal Conductivity-Nonmetallic Liquids and Gases”, Thermophysical and electronic properties information analysis center Lafayette in, 1970.

[30] A. Kumar, and T. DebRoy, “Toward a Unified Model to Prevent Humping Defects in Gas Tungsten Arc Welding,” *Welding Journal NewYork*, vol. 85, p. 292, 2006.

[31] C. Boley, S. A. Khairallah, and A. M. Rubenchik, “Calculation of Laser Absorption by Metal Powders in Additive Manufacturing,” *Applied Optics*, vol. 54, p. 2477-2482, 2015.

[32] X. Shu, B. A. L. Gwandu, Y. Liu et al., “Sampled Fiber Bragg grating for Simultaneous Refractive-Index and Temperature Measurement,” *Optics Letters*, vol. 26, p. 774-776, 2001.

[33] J.-H. Cho, and S.-J. Na, “Theoretical Analysis of Keyhole Dynamics in Polarized Laser Drilling,” *Journal of Physics D: Applied Physics*, vol. 40, p. 7638, 2007.